

UNIVERSITY OF BIRMINGHAM

Research at Birmingham

The Effect of Chemical Composition on High Temperature Behaviour of Fe and Cu Doped Mn-Co spinels

Masi, Andrea; Bellusci, Mariangela; McPhail, Stephen J.; Padella, Franco; Reale, Priscilla; Hong, Jong-Eun; Steinberger-Wilckens, Robert; Carlini, Maurizio

DOI:

[10.1016/j.ceramint.2016.11.135](https://doi.org/10.1016/j.ceramint.2016.11.135)

License:

Creative Commons: Attribution-NonCommercial-NoDerivs (CC BY-NC-ND)

Document Version

Peer reviewed version

Citation for published version (Harvard):

Masi, A, Bellusci, M, McPhail, SJ, Padella, F, Reale, P, Hong, J-E, Steinberger-Wilckens, R & Carlini, M 2017, 'The Effect of Chemical Composition on High Temperature Behaviour of Fe and Cu Doped Mn-Co spinels', *Ceramics International*, vol. 43, no. 2, pp. 2829-2835. <https://doi.org/10.1016/j.ceramint.2016.11.135>

[Link to publication on Research at Birmingham portal](#)

Publisher Rights Statement:

Checked 2/12/2016

General rights

Unless a licence is specified above, all rights (including copyright and moral rights) in this document are retained by the authors and/or the copyright holders. The express permission of the copyright holder must be obtained for any use of this material other than for purposes permitted by law.

- Users may freely distribute the URL that is used to identify this publication.
- Users may download and/or print one copy of the publication from the University of Birmingham research portal for the purpose of private study or non-commercial research.
- User may use extracts from the document in line with the concept of 'fair dealing' under the Copyright, Designs and Patents Act 1988 (?)
- Users may not further distribute the material nor use it for the purposes of commercial gain.

Where a licence is displayed above, please note the terms and conditions of the licence govern your use of this document.

When citing, please reference the published version.

Take down policy

While the University of Birmingham exercises care and attention in making items available there are rare occasions when an item has been uploaded in error or has been deemed to be commercially or otherwise sensitive.

If you believe that this is the case for this document, please contact UBIRA@lists.bham.ac.uk providing details and we will remove access to the work immediately and investigate.

1 **The Effect of Chemical Composition on High Temperature Behaviour of Fe and**
2 **Cu Doped Mn-Co spinels**

3 Andrea Masi ^{a,b,c}, Mariangela Bellusci ^a, Stephen J. McPhail ^a, Franco Padella ^a, Priscilla
4 Reale ^a, Jong-Eun Hong ^{b,1}, Robert Steinberger-Wilckens ^b, Maurizio Carlini ^c

5 ^a) ENEA C.R. Casaccia, 00123 Rome, Italy

6 ^b) School of Chemical Engineering, University of Birmingham, Edgbaston, Birmingham
7 B15 2TT, UK

8 ^c) University of Tuscia - DAFNE, 01100 Viterbo, Italy

9
10 *Corresponding Author: Andrea Masi, tel: +393394188284, fax +39 06 30486357, mail:
11 andrea.masi@enea.it, address: via Anguillarese 301, 00123, Roma (Italy)

12 ¹ Current address: Fuel Cell Laboratory, Korea Institute of Energy Research, 152
13 Gajeon-ro, Daejeon, xxxxx, Republic of Korea

14 Abstract

15 Mixed Mn-Co spinels are currently studied as protective coating materials for Solid
16 Oxide Fuel Cells interconnects. Compositional changes in manganese cobaltites lead to
17 modifications in the materials properties, such as sintering behaviour, thermal
18 expansion and electrical conductivity, with advantages in the technological application.
19 In this work, the effect of Fe, Cu and simultaneous Fe+Cu doping of Mn-Co spinels has
20 been studied. Different oxide powder mixtures were prepared with a High Energy Ball
21 Milling (HEBM) treatment, obtaining highly reactive oxides that easily form single
22 spinel phase compounds by moderate heating. The effect of the composition is observed
23 on high temperature stability of the spinel phase and on densification behaviour of the
24 powders, greatly enhanced by copper addition.

25 Analyses carried out on sintered pellets allow to observe simple relations among dopant
26 concentration, thermal expansion and electrical conductivity. The combined effect is
27 obtained in case of the simultaneous addition of multiple dopants. An appropriate
28 composition can be therefore designed to obtain a material characterized by enhanced
29 sintering behaviour, high electrical conductivity and tailored thermal expansion to fulfil
30 the application requirements.

31

32

33 **Keywords**

34 A. Milling B. Spinel C. Thermal expansion C. Electrical Conductivity

35 1. Introduction

36 Development and commercial breakthrough of Solid Oxide Fuel Cells (SOFCs) is
37 necessarily linked to reduction of costs and increase of long-term reliability. One of the
38 key-factors is represented by the substitution of ceramic interconnects with metallic
39 parts. High chromium ferritic steels have been identified as the most promising
40 candidate material because of their low cost and their Coefficient of Thermal Expansion
41 (CTE) compatibility with the SOFC materials [1]. In operating conditions, however,
42 long-term performance degradation arises due to the formation of insulating chromium-
43 rich oxides and the evaporation of volatile Cr species, that can migrate and react with
44 the cathode material, thereby reducing the active surface area [2]. The application of
45 protective coating is therefore mandatory to avoid these issues, and several materials are
46 being studied, including reactive element oxides, rare earth perovskite and spinel oxides
47 [3,4]. Among these materials, Mn-Co spinels with Co:Mn in the 1:1÷2:1 range,
48 characterized by high conductivity values and good thermal expansion compatibility
49 with ferritic stainless steels, have been suggested as the best candidates.
50 In view of large-scale application, cheap wet-powder coating techniques, such as spray
51 coating, screen printing and ink-jet printing, would be preferred. These methods rely on
52 their own ink formulations and sintering thermal treatments, and the effectiveness of the
53 coating is therefore related to efficient sintering steps. Sintering Mn-Co spinel powders
54 in air requires high temperature (e.g. 1000°C [5]), raising concerns about the
55 degradation of mechanical properties that could be induced in the substrate. To achieve
56 sufficient densification at lower temperature, thermal treatments in reducing atmosphere
57 are widely used, followed by oxidation steps to recover the spinel structure [6,7].
58 Alternatively, reduction of sintering temperature can be achieved with the introduction

59 of further elements acting as sintering aids, such as Cu and Ni [8,9], representing an
60 attractive approach avoiding a more expensive multi-step sintering treatment.

61 The addition of dopant elements, such as transition metals or reactive elements like Fe,
62 Ti, Cu, Ni or Y, has furthermore been proven effective in enhancing application related
63 to properties such as chromium retention capability or electrical conductivity [8,10,11].
64 However, changes in composition affect the thermal expansion behaviour: Mn-Co
65 spinels possess CTE values in the $9.7\div 13.5\cdot 10^{-6}\text{ K}^{-1}$ [12–15] and $10.6\div 14.1\cdot 10^{-6}\text{ K}^{-1}$
66 [5,8,10,16] ranges, respectively at 800°C and at 1000°C. Cu and Ni doping produces an
67 increase in CTE [8,9,14,15,17], while Fe and Ti lower this property [10]. No clear
68 relation between CTE and dopant concentration can be however deduced from the
69 literature, mostly due to the high dispersion of results. Furthermore, to the best of our
70 knowledge, no results have been reported related to the effect of simultaneous doping.

71 HEBM is a consolidated, cost effective and environmentally friendly powder processing
72 technique widely applied in material science. The technique consists in the exposure of
73 defined quantities of powder reactants to repeated energy transfer phenomena obtained
74 by colliding balls. The kinetic energy released from the balls to the powder can induce
75 several physico-chemical phenomena, the first being represented by fine grinding of
76 particles, and therefore formation of new active surfaces. Nanostructuring of the
77 powder can occur at this stage, enhancing significantly powder reactivity, followed by
78 interdiffusion, atomic rearrangements, nucleation of stable or metastable phases,
79 amorphization, re-crystallization phenomena and so on [18].

80 In our previous works, High Energy Ball Milling (HEBM) was evaluated as a synthesis
81 route to obtain mixed spinels starting from oxide powders [19,15]. A HEBM treatment
82 carried out on Mn-Co oxides promotes the room temperature solid state mechano-
83 chemical reaction between Mn and Co oxide mixtures, with a unitary reaction yield

84 after 65 h of milling. Powders obtained after relatively short mechano-chemical
85 treatments (e.g. 10 h), despite not containing a single phase compound, are
86 characterized by significantly enhanced reactivity with respect to pristine oxides, and
87 easily evolve to form the equilibrium products when subjected to moderate heating (i.e.
88 $T < 800^{\circ}\text{C}$).

89 In this work, to study the effect of Fe, Cu and simultaneous Fe+Cu doping on the
90 chemico-physical properties of Mn-Co spinels, different powder mixtures of Mn, Co, Fe
91 and Cu oxides are prepared and subjected to a HEBM treatment. The obtained highly
92 reactive powder samples are characterized in their thermal evolution and sintering
93 properties, and differences on powder densification behaviour and high temperature
94 spinel stability induced by the dopant contents are observed and reported. Finally, the
95 effect of different metal compositions on thermal expansion and electrical conductivity
96 of sintered samples is evaluated and discussed.

97

98 2. Experimental Procedure

99 Mn_3O_4 (Sigma Aldrich, 97%), Co_3O_4 (Sigma Aldrich, 99%), CuO (Carlo Erba, 99%)
100 and Fe_2O_3 (Carlo Erba, 99%) were mixed in stoichiometric quantities to obtain the
101 compositions reported and labelled in Table 1. The HEBM process was performed in a
102 SPEX8000M mixer mill, using cylindrical steel vials (60 cm^3 volume) and steel balls
103 (10mm diameter) with powder to balls weight ratio of 1:10. Vials were loaded with 8g
104 of powder, sealed in argon atmosphere and subjected to 10 hours of milling. After the
105 milling treatment, the absence of contamination from the milling media was assessed
106 evaluating chromium presence by means of energy-dispersive X-ray microanalysis
107 (Hitachi TM3030Plus).

108 X-Ray diffraction analyses (XRD) were carried out on a 120° angular dispersion X-ray
109 diffractometer (Italstructure, curved position sensitive detector from INEL), equipped
110 with Fe K_{α1} radiation source. Phase identification was performed on collected patterns
111 using the PDF-2 database [20] as reference data. Lorentzian fitting of selected
112 reflections allowed to evaluate cell parameters and to calculate accordingly theoretical
113 densities, considering nominal compositions of the samples.

114 Morphology of the samples was evaluated using N₂ adsorption at 77K technique
115 (Quantachrome Autosorb-iQ). Specific surface area (SSA) values were obtained by
116 applying the BET method [21]. BET particle size l was calculated as $l = \frac{6}{SSA \cdot \rho}$, where ρ
117 is the material density.

118 Thermogravimetric analysis was carried out in air using a Perkin Elmer thermobalance
119 (Pyris Diamond TG/DTA, Perkin Elmer) with the following procedure: heating scan up
120 to 1200°C at 5°C/min, 60 minutes of isothermal step and cooling to room temperature at
121 5°C/min.

122 Dilatometric measurements were performed in a push-rod dilatometer (DIL 402 C,
123 NETZSCH). To evaluate sintering behaviour, consolidated pellets of about 6mm
124 diameter length were obtained by uniaxial cold pressing (3.5 T/cm²) and heated in air
125 with a heating rate of 5°C/min up to 1200°C. Thermal expansion measurements were
126 carried out with a heating rate of 10°C/min on pellets of about 6mm diameter and
127 2.5mm height sintered as described later in the text. Average CTE was calculated
128 between room temperature and 800°C as: $CTE = \frac{1}{L_0} \frac{\Delta L}{\Delta T}$, where L_0 is the initial length and
129 ΔL represents the length change occurring in the ΔT temperature range.

130 To assess electrical conductivity, pellets of about 10mm diameter were obtained by
131 uniaxial cold pressing (3.5 T/cm²) and sintered similarly to thermal expansion samples.
132 The conductivity was measured by applying the Van der Pauw method [22] (PAR273A

133 potentiostat coupled to a HP 3457A multimeter) in the 500–800°C temperature range.

134 Activation energy E_a was calculated from the Arrhenius plot obtained using the

135 formula: $\sigma = \frac{\sigma_0}{T} e^{-\frac{E_a}{kT}}$, where σ is the conductivity, T the temperature, σ_0 the pre-

136 exponential factor, E_a the activation energy and k the Boltzmann's constant.

137 3. Results and discussion

138 3.1. Powder characterization

139 The XRD patterns of the 10 hours milled powders are reported in Fig. 1. All the

140 examined samples are characterized by similar patterns, with significant peak

141 broadening ascribable to nanostructuring of crystallites and strain. Starting with the

142 $\text{MnCo}_{1.8}\text{Fe}_{0.2}$ pattern, main peaks are ascribable to the presence of a cubic spinel

143 compound, compatible with Co_3O_4 phase (JCPDS card n. 42-1467). Peaks related to the

144 Mn_3O_4 compound are not evident, confirming that the cobalt rich phase exhibits a high

145 stability during the mechano-chemical treatment, as already observed in the case of

146 similar oxides mixtures [19,15]. The asymmetry of Co_3O_4 peaks towards lower angles

147 could be ascribed to the nucleation of a cubic spinel phase characterized by higher

148 lattice parameter, most likely a mixed spinel similar to MnCo_2O_4 (JCPDS card n. 23-

149 1237). The small broadened peaks at $2\theta \cong 48$ degrees is due to the presence of highly

150 destructured Fe_2O_3 phase (JCPDS card n. 33-0664), and are more evident in the

151 $\text{MnCo}_{1.6}\text{Fe}_{0.4}$ pattern, as expected due to the higher iron content. In the case of copper

152 containing samples, instead, clear evidences of CuO phase (JCPDS card n. 48-1548) are

153 not observed, suggesting low stability of CuO structure during the HEBM treatment,

154 most likely due to facile diffusion of small copper ions into the spinel lattice during the

155 mechano-chemical treatment. In the $\text{MnCo}_{1.6}\text{Fe}_{0.2}\text{Cu}_{0.2}$ pattern, similar to what is

156 observed for $\text{MnCo}_{1.8}\text{Fe}_{0.2}$ sample, features of a hematite phase are visible.

157 Therefore, as shown in the XRD analysis, the 10h HEBM treatment does not produce a
158 single equilibrium spinel phase but some metastable mixture of metal oxides.

159 Nitrogen adsorption measurements at 77K were carried out to calculate BET specific
160 surface area and thus evaluate the degree of particle aggregation. The obtained values
161 are reported in Table 2. Mn-Co-Fe samples exhibit comparable surface areas, while Cu
162 addition seems to favour higher degrees of aggregation resulting in lower surface areas.

163 The size of particles calculated with BET ranges between 160 and 330nm.

164 In order to evaluate the differences in the high temperature behaviour of the powders,
165 which is induced by the cobalt substitution, thermogravimetric analyses up to 1200°C
166 were carried out and are reported in Fig. 2. The samples exhibit an initial weight loss,
167 ascribable to adsorbed humidity departure. In the 200–500°C temperature range a
168 weight gain step is instead observed. This phenomenon can be related to the powder
169 comminution and activation induced by the HEBM, carried out in Ar atmosphere.

170 Highly reactive new surfaces are produced during the mechano-chemical treatment that
171 interacts with oxygen already at low temperature giving rise to the oxidation
172 phenomena observed during the thermal treatment. Moreover, the HEBM treatment
173 induces a high degree of interdiffusion of the precursor oxides with solid state reactions
174 at the new interfaces, most likely with the formation of highly anion defective lattices,
175 due to the milling atmosphere. Subsequent filling of the oxygen vacancies may
176 therefore occur when exposed to air at moderate temperatures. The occurrence of
177 similar weight gain phenomena and the existence of metastable non-stoichiometric
178 mixed valence spinels has been observed for similar systems and ascribed to high
179 reactivity due to high nanostructuring of the compounds [23], and it is supposed that
180 similar mechanisms occur here, due to the defectivity induced by the HEBM treatment.

181 Regarding the influence of the composition on this weight gain step, it can be observed
182 that the magnitude of the weight gain increases following the order: $\text{MnCo}_{1.6}\text{Fe}_{0.4}$
183 $< \text{MnCo}_{1.8}\text{Fe}_{0.2} < \text{MnCo}_{1.6}\text{Fe}_{0.2}\text{Cu}_{0.2} < \text{MnCo}_{1.8}\text{Cu}_{0.2}$. This can be related to the
184 initial powder composition: Co_3O_4 precursor is substituted with species characterized by
185 different oxygen content (i.e. Fe_2O_3 and CuO), and it is likely to suppose that, with Fe
186 and Cu ions presence in the spinel lattice due to the mechano-chemical treatment, the
187 oxygen uptake of the metastable spinels will be inversely related to the initial oxygen
188 content.

189 Following this weight gain step, in the 500–700°C temperature range a gradual weight
190 loss can be observed, related to the rearrangement and homogenization of the oxidized
191 compound to form the expected high temperature single spinel phase. At about 800°C,
192 in fact, the curves reach a plateau, suggesting that no further oxygen release occurs.

193 Also in this weight change step a relationship between the weight loss and the material
194 composition can be observed: in particular, the weight loss increases following the order:
195 $\text{MnCo}_{1.8}\text{Cu}_{0.2} < \text{MnCo}_{1.6}\text{Fe}_{0.2}\text{Cu}_{0.2} < \text{MnCo}_{1.8}\text{Fe}_{0.2} < \text{MnCo}_{1.6}\text{Fe}_{0.4}$. The samples
196 characterized by the higher initial oxygen content show therefore the higher mass loss.

197 The substitution of the $\text{Co}^{2+}/\text{Co}^{3+}$ precursor with higher or lower oxidation state species,
198 respectively Fe^{3+} from Fe_2O_3 and Cu^{2+} from CuO , affects the oxidation behaviour of the
199 milled powder both during the formation of the metastable spinels and during the
200 homogenization reaction that produce equilibrium compounds. In our previous work
201 [19], we observed that during mechano-chemical treatment of Mn and Co oxides the
202 reaction proceeds through nucleation and growth of mixed phases rather than through
203 interdiffusion phenomena of the starting oxides. Observing how the thermal behaviour
204 of the doped powders is influenced by the initial composition, it is likely to suppose that

205 the formation of Fe and Cu doped phases occurs already during the milling step,
206 suggesting that a similar reaction mechanism is involved.

207 Further increase of temperature above 1000°C leads to a third weight loss phenomenon,
208 that can be related to metal reduction from the spinel phases with related oxygen
209 release, due to the formation of Me(II) oxide phases. The existence of a high
210 temperature spinel-Me^{II}O multi-phase boundary is known for Co-Mn oxide mixtures
211 [24], and the data reported here suggest that a similar behaviour is retained with Fe and
212 Cu addition to the spinel composition, with some differences in the onset temperature.
213 Co substitution with Fe appears to extend the spinel stability region. Copper substitution
214 promotes instead the spinel de-mixing at lower temperature.

215 During the successive cooling stage, the weight loss associated to the high temperature
216 phase transition is recovered for all the stoichiometries, compatibly with spinel stability
217 at intermediate temperature. In the case of the MnCo_{1.8}Cu_{0.2} sample, weight gain
218 occurs in two steps, suggesting a multiple oxidation process that could be due to
219 multiple high temperature dual-phase regions, as observable in the Cu-Co oxides phase
220 diagram [25].

221 To evaluate sintering behaviour, consolidated pellets were formed with the 10h HEBM
222 powders. The pre-sintering densities are reported in Table 3: similar values of density
223 are obtained for all the different samples, as expected from the processing of
224 morphologically similar powders. Shrinkage and shrinkage rate curves are reported in
225 Fig. 3. Mn-Co-Fe samples show behaviour comparable to similar Mn-Co spinels [15],
226 with sintering temperatures of about 1040–1060°C and maximum densification rates at
227 1150°C approximately. The addition of Cu significantly improves sintering: in the case
228 of MnCo_{1.8}Cu_{0.2} and MnCo_{1.6}Fe_{0.2}Cu_{0.2} samples, shrinkage starts at approximately
229 925–950°C, with maximum densification rate occurring at $T \cong 1000^\circ\text{C}$.

230 XRD analysis carried out on the pellets after dilatometric measurements indicated
231 however the presence of secondary phases: differently with respect to
232 thermogravimetric measurements, thermal treatment of the pellets at 1200°C could
233 result in the lack of recovery of the single spinel structure upon cooling. This is most
234 likely due to high packing and higher crystals growth, limiting oxygen diffusion. Being
235 crucial to obtain single phase pellets to evaluate precisely thermal expansion and
236 electrical conductivity properties, different sintering procedures were studied to obtain
237 dense single phase pellets. In the case of the $\text{MnCo}_{1.8}\text{Fe}_{0.2}$ and $\text{MnCo}_{1.6}\text{Fe}_{0.4}$ sample,
238 requiring sintering temperature of 1200°C to achieve high density values, a lower
239 temperature (800°C) dwell step was introduced to facilitate spinel recovery. The
240 significantly lower sintering temperature of Cu containing compounds, as evidenced by
241 dilatometric analysis, allowed to reduce the maximum treatment temperature to 1000°C
242 still obtaining dense pellets.

243 The sintered densities obtained for the different samples, reported in Table 3, show how
244 Cu inclusion leads to a significant enhancement of densification: Cu substituted samples
245 are in fact characterized by higher density with respect to Mn-Co-Fe samples even with
246 a reduction in sintering temperature of 200K.

247 X-Ray diffraction patterns of the sintered samples are reported in Fig. 4. All
248 compositions exhibit a single cubic spinel phase. The evidence of well-defined peaks
249 suggests a significant crystal growth during the sintering process. Peak shifts with
250 respect to the standard MnCo_2O_4 phase are observed for the different compositions,
251 highlighted by the calculated cell parameters reported in Table 4. In particular, due to
252 the different size of dopants ionic radius with respect to the substituted cobalt [26], Fe-
253 Co substitution promotes the enlargement of the lattice (8.27Å for MnCo_2O_4 [20]),

254 differently from Cu-Co substitution that, due to similar ionic radii, does not induce
255 significant changes in the cell parameter.

256

257 3.2. Thermal expansion

258 Thermal expansion compatibility between the substrate and the coating material is a
259 crucial factor to avoid mechanical stress that could arise during thermal cycles or long
260 term operation and could promote cracking or delamination of the coatings. To evaluate
261 CTE of the examined materials, the sintered pellets were subjected to dilatometric
262 analyses. In Fig. 5 the expansion curves are reported, and average CTE values
263 calculated between room temperature and 800°C are listed in Table 5. All the samples
264 exhibit a linear behaviour through all the measured temperature range. The results here
265 obtained are comparable to values found in literature for similar compounds (e.g. [10]).
266 Considering the thermal expansion of ferritic stainless steels, i.e. $11\text{--}13 \cdot 10^{-6} \text{K}^{-1}$ [27],
267 MnCo_{1.8}Cu_{0.2} samples possess lower compatibility with respect to the Fe containing
268 samples.

269 To evaluate how cobalt substitution with Fe and Cu affects this property, in Fig. 6 are
270 depicted the CTE values at 800°C versus the cobalt content for the different samples,
271 compared with result previously obtained on a MnCo₂O₄ spinel [15]. It can be observed
272 a clear negative trend between CTE value and iron content, while MnCo_{1.8}Cu_{0.2}
273 sample is characterized by higher CTE value than the undoped sample. Consistently
274 with the single metal doped samples, the combined effect is obtained in the
275 MnCo_{1.6}Fe_{0.2}Cu_{0.2} compound, the CTE of which is ranged between those of
276 MnCo_{1.8}Fe_{0.2} and MnCo_{1.8}Cu_{0.2}. This result suggests that the CTE of Mn-Co spinels
277 can be tuned in the examined range by compositional tailoring, as the effect of the

278 cobalt substitution with copper and iron on CTE is retained with the simultaneous
279 doping.

280 Regarding the dependence of the CTE with the composition, the obtained results are in
281 agreement with previous studies that suggest the occurrence of a relation between CTE
282 and the different occupations and valence states in the spinel lattice [28]. In particular,
283 mixed element spinels characterized by higher valence differences among the sites
284 possess higher CTE, especially when this difference occurs between octahedrally
285 coordinated cations [28]. In Mn-Co spinels, tetrahedral sites are occupied preferentially
286 by Co^{II} species, while octahedral sites are occupied by Co^{II} , Co^{III} , Mn^{III} and Mn^{IV} . The
287 amount of Co^{II} and Mn^{IV} , strictly connected due to charge neutrality restraints, is
288 maximum when $\text{Co}:\text{Mn}\sim 2$ [29]. The substitution of Co with Fe occurs with Fe^{III} species
289 occupying preferentially octahedral sites in place of Co atoms [11], reducing the amount
290 of octahedral Co^{II} and therefore the amount of species characterized by different
291 valences. When copper is added to the compound, instead, Cu atoms tend to occupy
292 preferentially tetrahedral sites [30], with the presence of Cu^{I} and Cu^{II} species.

293 Moreover, copper addition is likely to promote octahedral Mn^{III} oxidation to Mn^{IV} to
294 maintain charge neutrality [30], increasing further the number of different valence
295 species in the lattice and therefore CTE.

296 When Co is substituted by both Fe and Cu, the enhancement of CTE due to Cu^{I} and Cu^{II}
297 introduction on tetrahedral sites is counterbalanced by the CTE decrease induced by the
298 Fe^{III} presence in octahedral sites, and, with Fe and Cu ions not being competitors for
299 lattice sites occupation in the examined composition range, the overall CTE change can
300 be considered as limited to the sum of the single dopants contributions.

301

302 3.3. Electrical conductivity

303 Electrical conductivity was evaluated by means of Van der Pauw method in the
304 temperature range 500–800°C. In Fig. 7 the Arrhenius plots are reported. All samples
305 exhibit a linear relation: evaluating the slope of the linear fits to the Arrhenius curves
306 activation energy was calculated, and results are reported in Table 6. All samples show
307 similar values of about 0.5eV, suggesting a similar conduction mechanism.

308 In Fig. 8 the conductivity values measured at 800°C for the different samples are
309 reported as a function of the cobalt content, and compared with an undoped MnCo_2O_4
310 spinel [15]. It can be observed a clear decreasing trend upon the substitution of Co with
311 Fe, with conductivity of about 51 S/cm and 36 S/cm for $\text{MnCo}_{1.8}\text{Fe}_{0.2}$ and
312 $\text{MnCo}_{1.6}\text{Fe}_{0.4}$ samples respectively. Co substitution with Cu significantly increases
313 conductivity, and similar enhancements are observed when cobalt is substituted in the
314 reference material ($\text{Mn}_{1.8}\text{Co}_{1.8}\text{Cu}_{0.2}$ versus MnCo_2O_4) or in the iron doped sample
315 ($\text{MnCo}_{1.6}\text{Fe}_{0.2}\text{Cu}_{0.2}$ versus $\text{Mn}_{1.8}\text{Co}_{1.8}\text{Fe}_{0.2}$).

316 The electrical conductivity in spinels is associated with a small polaron hopping
317 mechanism between mixed valence elements on octahedral sites and in Mn-Co oxides it
318 is related to $\text{Co}^{\text{II}}/\text{Co}^{\text{III}}$ and $\text{Mn}^{\text{III}}/\text{Mn}^{\text{IV}}$ pairs [13,28]. The valence state concentration
319 ratio affects therefore significantly conductivity properties. The observed decrease in
320 conductivity with Fe substitution is related to the preferential occupation of octahedral
321 sites by Fe^{III} atoms, not involved in polaron formation, limiting the charge carrier
322 density [11]. Regarding Cu addition, the conductivity enhancement could be due to
323 multiple factors: the aforementioned promotion of Mn^{III} oxidation to Mn^{IV} to maintain
324 charge neutrality [30], occurring with the presence of Cu^{I} and Cu^{II} species in the lattice,
325 could increase the number of active pairs on octahedral sites. Furthermore, Cu atoms in
326 tetrahedral sites could contribute indirectly through mediation of charge transfers

327 between close Mn atoms in octahedral sites [31]. The electrical conductivity
328 enhancement observed with copper addition therefore could be attributed to an indirect
329 enhancement of Mn pairs contribution.

330 Similarly to what was observed for CTE, most likely due to the absence of competition
331 for lattice site occupation among the dopants, our results suggest that the effect of the
332 simultaneous substitution is limited to the sum of the single factors.

333

334 4. Conclusions

335 Doped spinels were successfully produced by a mechano-chemically enhanced solid
336 state reaction synthesis. The effect of doping has been clearly highlighted with respect
337 to high temperature stability, sintering behaviour, CTE and electrical conductivity.

338 Through a high energy ball milling treatment, Fe and Cu substituted Mn-Co highly
339 reactive oxide mixtures were obtained. The powders easily form the expected single
340 cubic phase when exposed to moderate temperature ($T < 800^{\circ}\text{C}$). Influence of the dopant
341 content was observed on thermal stability of the spinel phase, enhanced by Fe and
342 decreased by Cu addition.

343 Regarding the densification behaviour, Cu addition resulted highly effective in reducing
344 sintering temperature and achieving higher density at lower temperature, while iron
345 doping did not lead to significant improvement with respect to the undoped Mn-Co
346 sample.

347 The measurement of thermal expansion of the sintered pellets indicated a direct relation
348 between Co substitution and CTE, which decreased with Fe content and was increased
349 by Cu doping. The sample substituted with both Cu and Fe revealed a combined effect
350 on CTE, ranged between that of Fe or Cu doped sample. Similar influence of the
351 composition was observed also on electrical conductivity, lowered by Fe doping and

352 greatly enhanced by Cu addition, with the mixed Cu-Fe-Mn-Co sample behaving
353 coherently.
354 Substitution of Co with Fe and Cu to obtain a Fe-Cu doped Mn-Co spinel proved
355 therefore as a versatile approach to enhance sintering behaviour and electrical
356 conductivity while retaining thermal expansion compatibility with ferritic stainless
357 steels. This suggests that a multiple doping approach can represent an effective strategy
358 to design cobaltite materials properly tailored on the application.

359

360 5. Acknowledgments

361 This work is supported by the FCH JU within the project SCORED 2:0 under contract.
362 325331. The authors wish to thank Dr. Claudia Paoletti for the technical support and
363 useful discussions.

364

365 Bibliography

- 366 [1] W.Z. Zhu, S.C. Deevi, Development of interconnect materials for solid oxide
367 fuel cells, *Mater. Sci. Eng. A.* 348 (2003) 227–243. doi:10.1016/S0921-5093(02)00736-
368 0.
- 369 [2] K. Hilpert, Chromium Vapor Species over Solid Oxide Fuel Cell Interconnect
370 Materials and Their Potential for Degradation Processes, *J. Electrochem. Soc.* 143
371 (1996) 3642. doi:10.1149/1.1837264.
- 372 [3] N. Shaigan, W. Qu, D.G. Ivey, W. Chen, A review of recent progress in
373 coatings, surface modifications and alloy developments for solid oxide fuel cell ferritic
374 stainless steel interconnects, *J. Power Sources.* 195 (2010) 1529–1542.
375 doi:10.1016/j.jpowsour.2009.09.069.
- 376 [4] J. Wu, X. Liu, Recent Development of SOFC Metallic Interconnect, *J. Mater.*
377 *Sci. Technol.* 26 (2010) 293–305. doi:10.1016/S1005-0302(10)60049-7.
- 378 [5] M.Y. Yoon, E.J. Lee, R.H. Song, H.J. Hwang, Preparation and properties of a
379 MnCo₂O₄ for ceramic interconnect of solid oxide fuel cell via glycine nitrate process,
380 *Met. Mater. Int.* 17 (2011) 1039–1043. doi:10.1007/s12540-011-6025-5.
- 381 [6] Z. Yang, G.G. Xia, G.D. Maupin, J.W. Stevenson, Conductive protection layers
382 on oxidation resistant alloys for SOFC interconnect applications, *Surf. Coatings*
383 *Technol.* 201 (2006) 4476–4483. doi:10.1016/j.surfcoat.2006.08.082.
- 384 [7] X. Montero, F. Tietz, D. Sebold, H.P. Buchkremer, a. Ringuede, M. Cassir, a.
385 Laresgoiti, I. Villarreal, MnCo_{1.9}Fe_{0.1}O₄ spinel protection layer on commercial ferritic
386 steels for interconnect applications in solid oxide fuel cells, *J. Power Sources.* 184
387 (2008) 172–179. doi:10.1016/j.jpowsour.2008.05.081.

- 388 [8] B.-K. Park, J.-W. Lee, S.-B. Lee, T.-H. Lim, S.-J. Park, C.-O. Park, R.-H. Song,
389 Cu- and Ni-doped $Mn_{1.5}Co_{1.5}O_4$ spinel coatings on metallic interconnects for solid
390 oxide fuel cells, *Int. J. Hydrogen Energy*. 38 (2013) 12043–12050.
391 doi:10.1016/j.ijhydene.2013.07.025.
- 392 [9] Y. Xu, Z. Wen, S. Wang, T. Wen, Cu doped Mn–Co spinel protective coating on
393 ferritic stainless steels for SOFC interconnect applications, *Solid State Ionics*. 192
394 (2011) 561–564. doi:10.1016/j.ssi.2010.05.052.
- 395 [10] K. Wang, Y. Liu, J.W. Fergus, Interactions between SOFC interconnect coating
396 materials and chromia, *J. Am. Ceram. Soc.* 94 (2011) 4490–4495. doi:10.1111/j.1551-
397 2916.2011.04749.x.
- 398 [11] Y. Liu, J.W. Fergus, K. Wang, C. Dela Cruz, Crystal Structure, Chemical
399 Stabilities and Electrical Conductivity of Fe-Doped Manganese Cobalt Spinel Oxides
400 for SOFC Interconnect Coatings, *J. Electrochem. Soc.* 160 (2013) F1316–F1321.
401 doi:10.1149/2.114311jes.
- 402 [12] Z. Yang, G.-G. Xia, X.-H. Li, J.W. Stevenson, $(Mn,Co)_3O_4$ spinel coatings on
403 ferritic stainless steels for SOFC interconnect applications, *Int. J. Hydrogen Energy*. 32
404 (2007) 3648–3654. doi:10.1016/j.ijhydene.2006.08.048.
- 405 [13] A. Petric, H. Ling, Electrical Conductivity and Thermal Expansion of Spinel at
406 Elevated Temperatures, *J. Am. Ceram. Soc.* 90 (2007) 1515–1520. doi:10.1111/j.1551-
407 2916.2007.01522.x.
- 408 [14] G. Chen, X. Xin, T. Luo, L. Liu, Y. Zhou, C. Yuan, C. Lin, Z. Zhan, S. Wang,
409 $Mn_{1.4}Co_{1.4}Cu_{0.2}O_4$ spinel protective coating on ferritic stainless steels for solid oxide
410 fuel cell interconnect applications, *J. Power Sources*. 278 (2015) 230–234.
411 doi:10.1016/j.jpowsour.2014.12.070.

- 412 [15] A. Masi, M. Bellusci, S.J. McPhail, F. Padella, P. Reale, J. Hong, R.
413 Steinberger-Wilckens, M. Carlini, Cu-Mn-Co oxides as protective materials in SOFC
414 technology: The effect of chemical composition on mechanochemical synthesis,
415 sintering behaviour, thermal expansion and electrical conductivity, *J. Eur. Ceram. Soc.*
416 37 (2017) 661–669. doi:10.1016/j.jeurceramsoc.2016.09.025.
- 417 [16] Y. Liu, J.W. Fergus, C. Dela Cruz, Electrical properties, cation distributions, and
418 thermal expansion of manganese cobalt chromite spinel oxides, *J. Am. Ceram. Soc.* 96
419 (2013) 1841–1846. doi:10.1111/jace.12254.
- 420 [17] J. Xiao, W. Zhang, C. Xiong, B. Chi, J. Pu, L. Jian, Oxidation of
421 MnCu_{0.5}Co_{1.5}O₄ spinel coated SUS430 alloy interconnect in anode and cathode
422 atmospheres for intermediate temperature solid oxide fuel cell, *Int. J. Hydrogen Energy.*
423 40 (2015) 1868–1876. doi:10.1016/j.ijhydene.2014.11.124.
- 424 [18] P. Baláž, M. Achimovičová, M. Baláž, P. Billik, Z. Cherkezova-Zheleva, J.M.
425 Criado, F. Delogu, E. Dutková, E. Gaffet, F.J. Gotor, R. Kumar, I. Mitov, T. Rojac, M.
426 Senna, A. Streletskii, K. Wieczorek-Ciurowa, Hallmarks of mechanochemistry: from
427 nanoparticles to technology, *Chem. Soc. Rev.* 42 (2013) 7571. doi:10.1039/c3cs35468g.
- 428 [19] A. Masi, M. Bellusci, M. Carlini, S.J. McPhail, F. Padella, P. Reale,
429 Mechanochemical Processing of Mn and Co Oxides: An Alternative Way to Synthesize
430 Mixed Spinel for Protective Coating, *J. Am. Ceram. Soc.* 99 (2016) 308–314.
431 doi:10.1111/jace.13863.
- 432 [20] ICPDS.ICDD, -, PCPDF-WIN Version 2.01. (1998).
- 433 [21] S. Brunauer, P.H. Emmett, E. Teller, Adsorption of Gases in Multimolecular
434 Layers, *J. Am. Chem. Soc.* 60 (1938) 309–319. doi:10.1021/ja01269a023.

435 [22] L.J. van der Pauw, A method of measuring the resistivity and Hall coefficient on
436 lamellae of arbitrary shape, Philips Tech. Rev. 20 (1958) 220–224.

437 [23] B. Gillot, DTG Curves of Selective Oxidation of Submicrometer Mixed Valency
438 Spinel: Data Table for the Oxidation Temperature of Transition Metals and Its Relation
439 to the Cation-Oxygen Distance, J. Solid State Chem. 113 (1994) 163–167.
440 doi:10.1006/jssc.1994.1355.

441 [24] E. Aukrust, A. Muan, Phase Relations in the System Cobalt Oxide-Manganese
442 Oxide in Air, J. Am. Ceram. Soc. 46 (1963) 511–511. doi:10.1111/j.1151-
443 2916.1963.tb13790.x.

444 [25] L. a. Zabdyr, O.B. Fabrichnaya, Phase equilibria in the cobalt oxide-copper
445 oxide system, J. Phase Equilibria. 23 (2002) 149–155. doi:10.1361/1054971023604161.

446 [26] R.D. Shannon, Revised effective ionic radii and systematic studies of
447 interatomic distances in halides and chalcogenides, Acta Crystallogr. Sect. A. 32 (1976)
448 751–767. doi:10.1107/S0567739476001551.

449 [27] Z. Yang, K.S. Weil, D.M. Paxton, J.W. Stevenson, Selection and Evaluation of
450 Heat-Resistant Alloys for SOFC Interconnect Applications, J. Electrochem. Soc. 150
451 (2003) A1188. doi:10.1149/1.1595659.

452 [28] G. Bayer, Thermal expansion of oxide compounds with spinel structure,
453 Thermochem. Acta. 3 (1972) 421–426. doi:10.1016/0040-6031(72)85001-9.

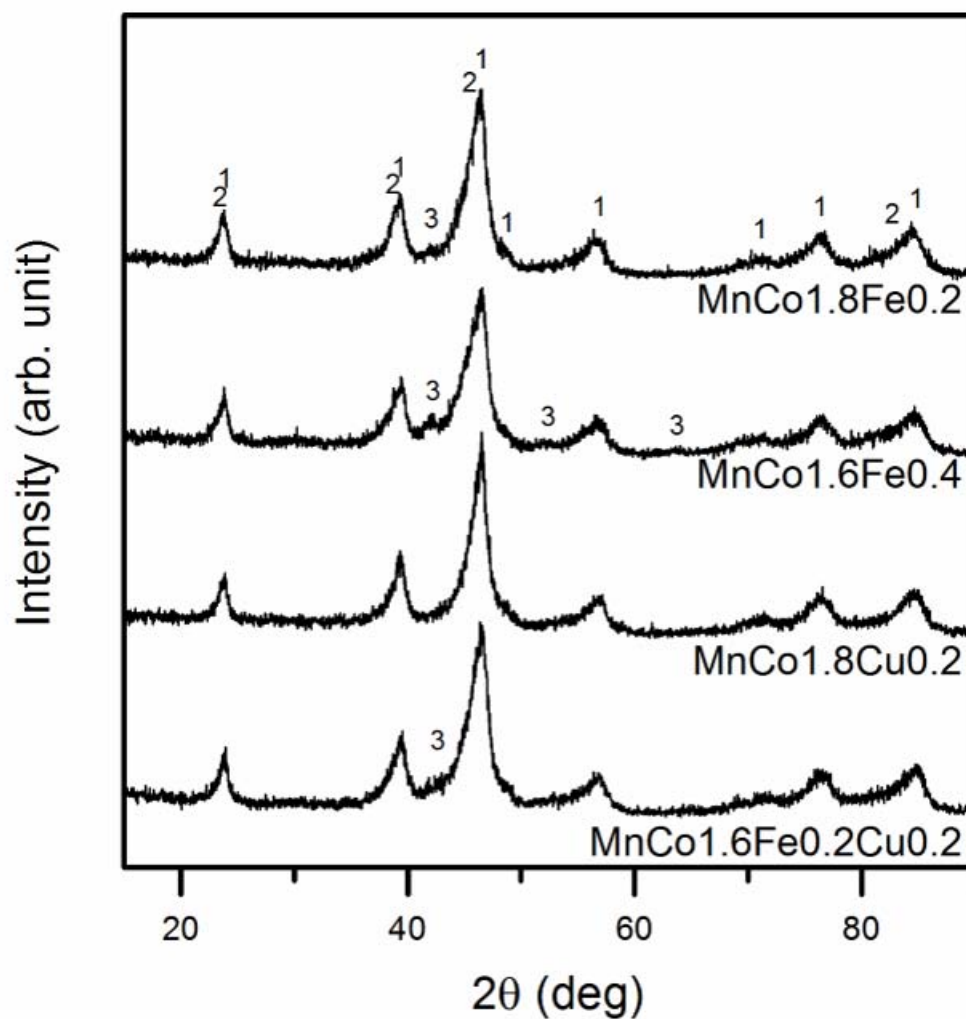
454 [29] H. Bordeneuve, C. Tenailleau, S. Guillemet-Fritsch, R. Smith, E. Suard, A.
455 Rousset, Structural variations and cation distributions in $Mn_{3-x}Co_xO_4$ ($0 \leq x \leq 3$) dense
456 ceramics using neutron diffraction data, Solid State Sci. 12 (2010) 379–386.
457 doi:10.1016/j.solidstatesciences.2009.11.018.

458 [30] P. a. Wright, S. Natarajan, J.M. Thomas, P.L. Gai-Boyes, Mixed-metal
459 amorphous and spinel phase oxidation catalysts: characterization by x-ray diffraction, x-
460 ray absorption, electron microscopy, and catalytic studies of systems containing copper,
461 cobalt, and manganese, *Chem. Mater.* 4 (1992) 1053–1065. doi:10.1021/cm00023a024.

462 [31] E. Elbadraoui, Cation distribution and mechanism of electrical conduction in
463 nickel-copper manganite spinels, *Solid State Ionics.* 93 (1997) 219–225.
464 doi:10.1016/S0167-2738(96)00559-0.

465

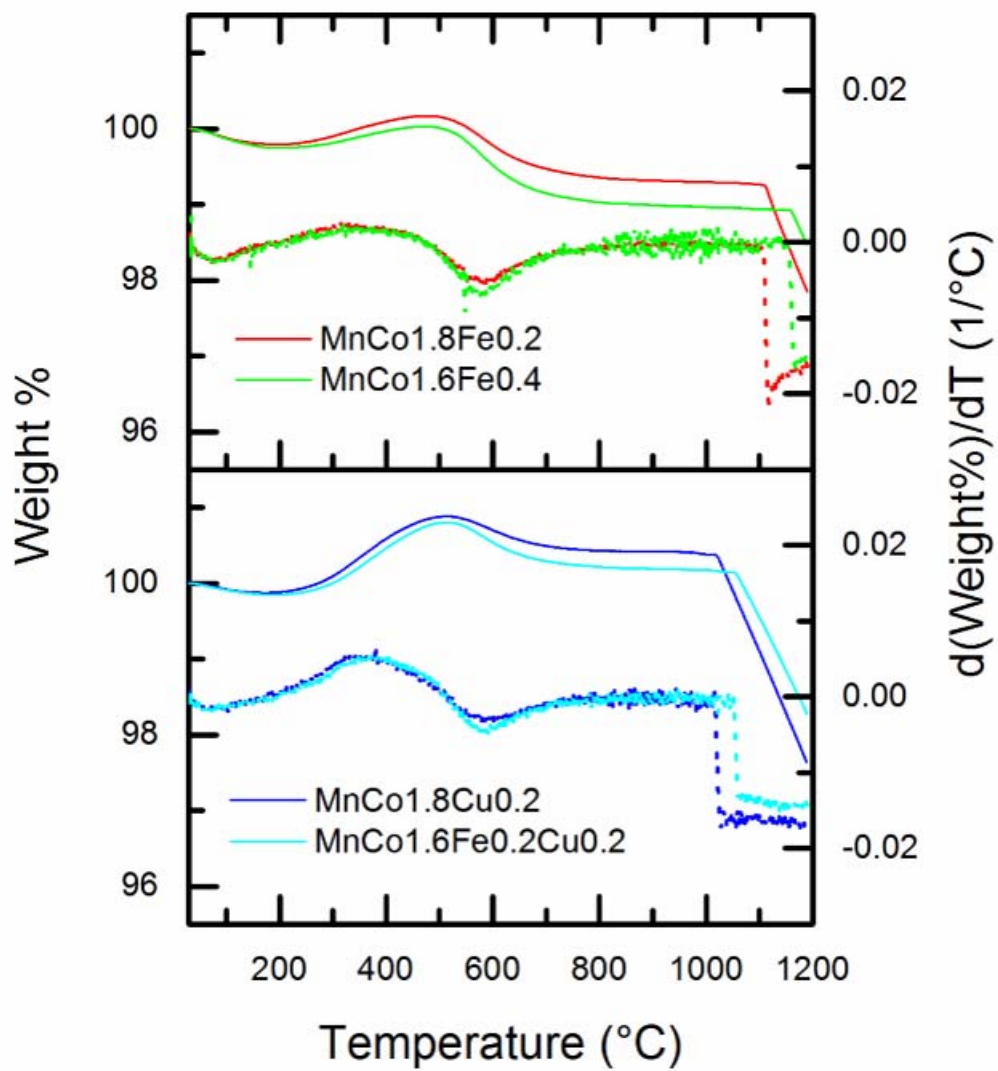
466



468

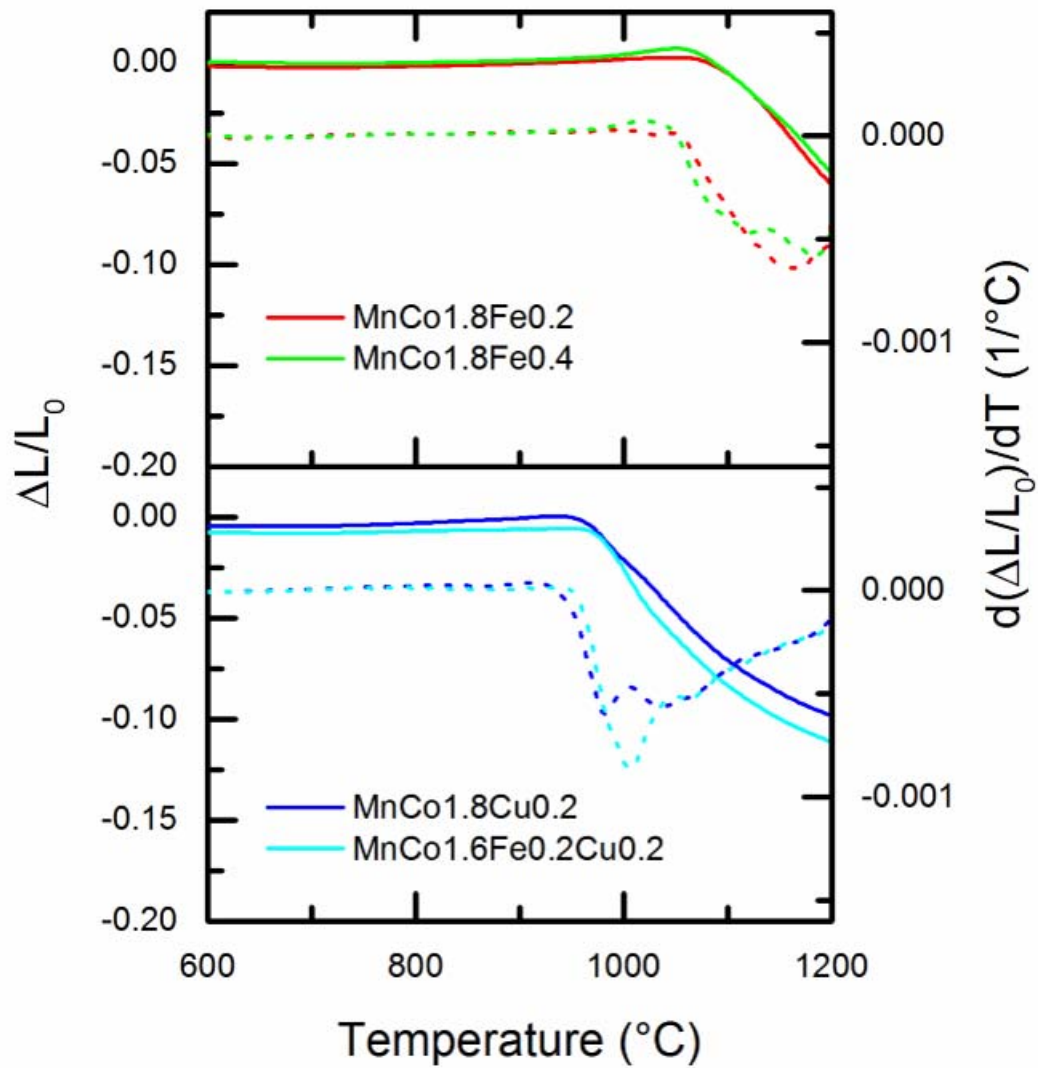
469 *Fig. 1. X-ray powder diffraction patterns of the different samples after 10h of milling;*

470 *1) Co₃O₄ 2) MnCo₂O₄ 3) Fe₂O₃ reflections.*



471

472 *Fig. 2. Thermogravimetric curves as a function of temperature for the different*
 473 *samples; solid lines represent weight% change, dotted lines the derivative of wright%*
 474 *versus temperature.*

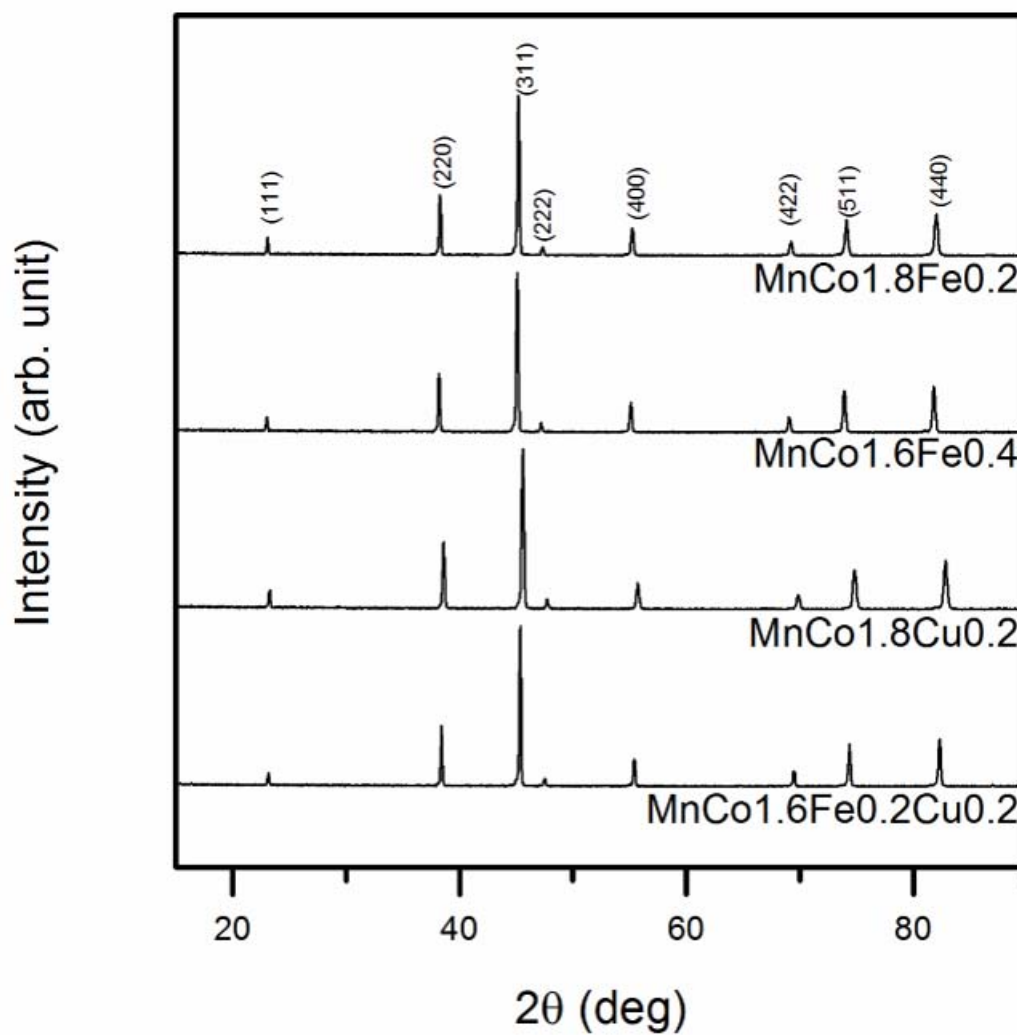


475

476 *Fig. 3. Dilatometric curves as a function of temperature of the different samples; solid*

477 *lines represent the length change, dashed lines the derivative of the length change*

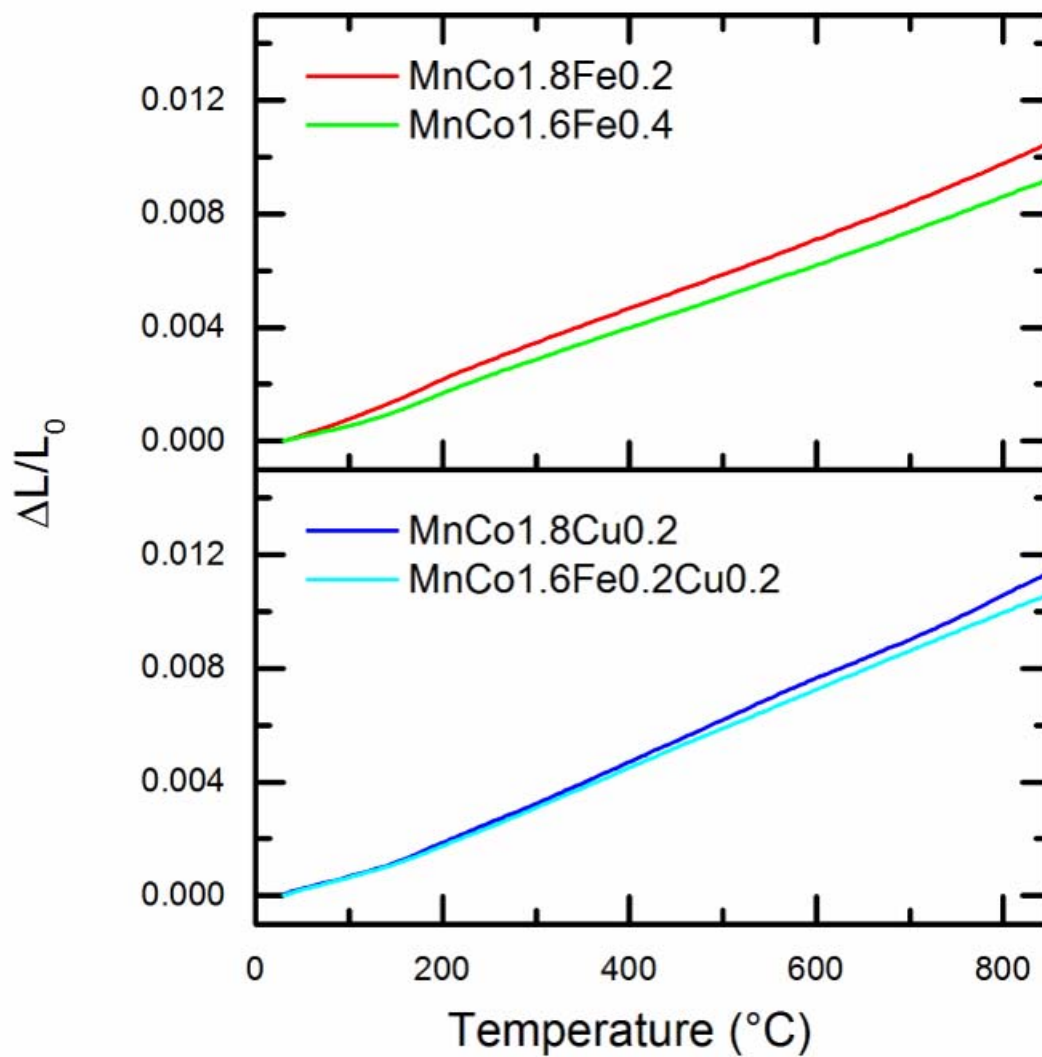
478 *versus temperature.*



479

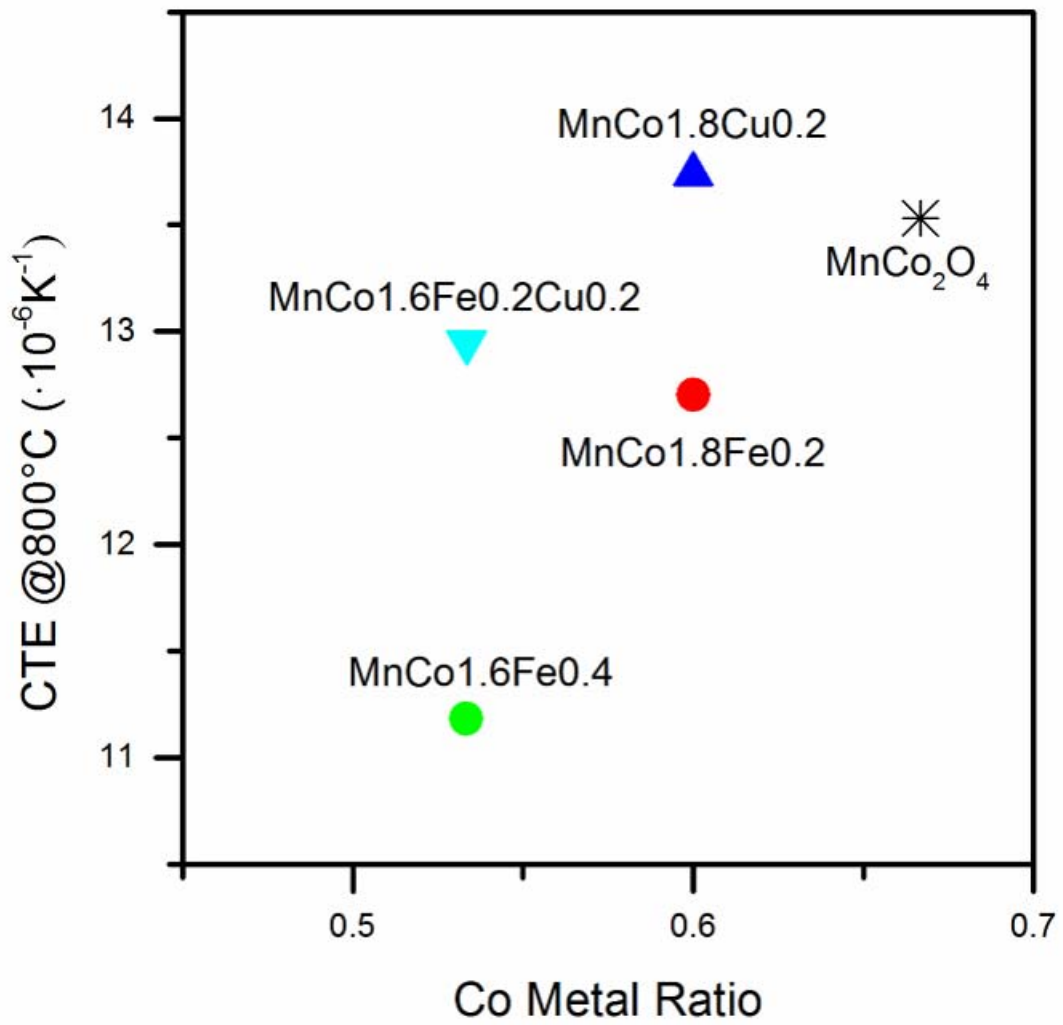
480 *Fig. 4. X-ray powder diffraction patterns of the samples after sintering treatment;*

481 *specified reflections are ascribable to a cubic spinel phase.*



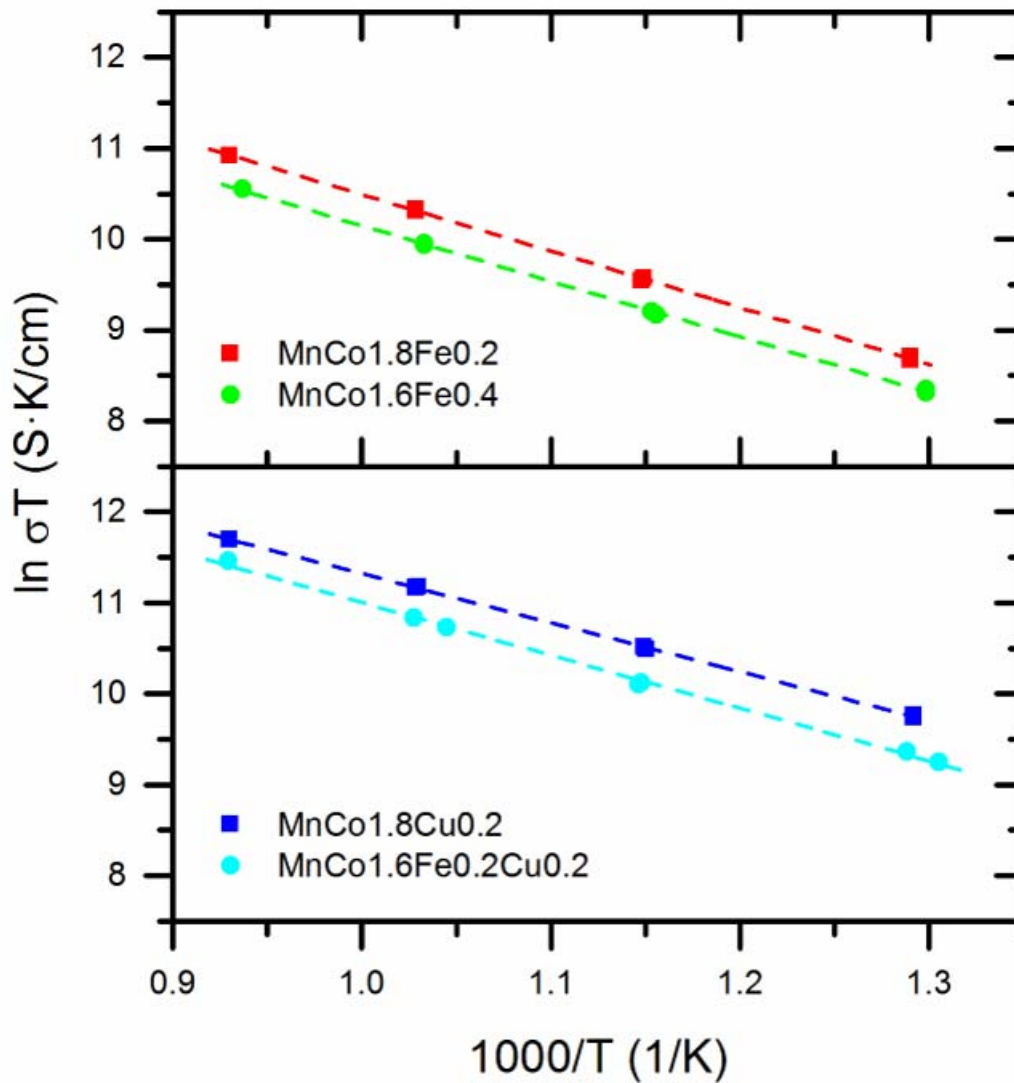
482

483 *Fig. 5. Thermal expansion curves of the sintered samples.*



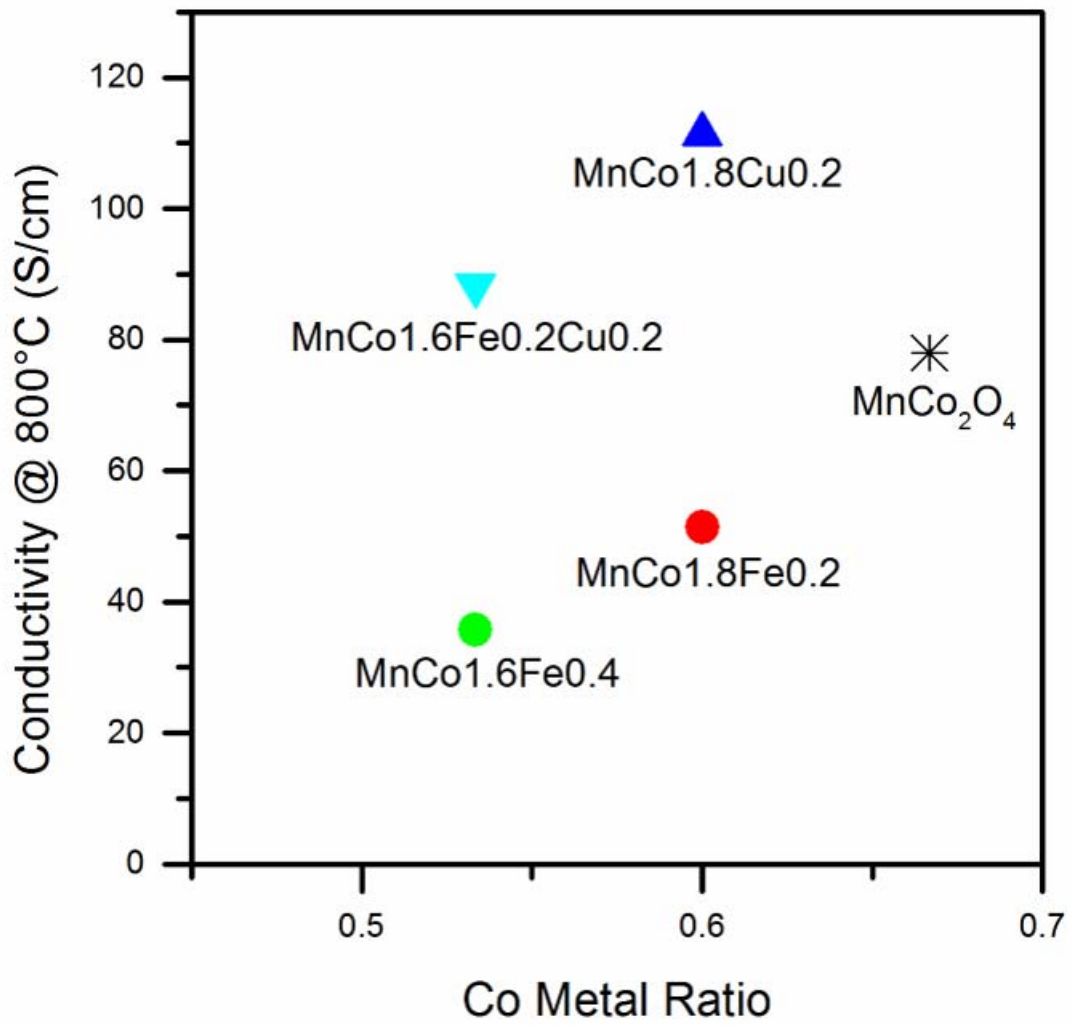
484

485 *Fig. 6. Coefficient of thermal expansion calculated at 800°C as a function of the Cobalt*
 486 *substitution in comparison with the undoped material (as reported in [15]).*



487

488 *Fig. 7: Arrhenius plots of electrical conductivity measured (dots) for the different*
 489 *samples and linear fits of the experimental points (dashed lines).*



490

491 *Fig. 8. Conductivity values measured at 800°C as a function of the Cobalt substitution*
 492 *in comparison with the undoped material (as reported in [15]).*

493

494

495 Tables
 496

497 Table 1: Sample nomenclature and nominal composition.

Sample name	Atomic ratio				Nominal composition
	Mn	Co	Fe	Cu	
MnCo1.8Fe0.2	0.33	0.60	0.07		MnCo _{1.8} Fe _{0.2} O ₄
MnCo1.6Fe0.4	0.33	0.53	0.14		MnCo _{1.6} Fe _{0.4} O ₄
MnCo1.8Cu0.2	0.33	0.60		0.07	MnCo _{1.8} Cu _{0.2} O ₄
MnCo1.6Fe0.2Cu0.2	0.33	0.53	0.07	0.07	MnCo _{1.6} Fe _{0.2} Cu _{0.2} O ₄

498

499

500 Table 2: BET surface area and BET particle size for the 10h HEBM powders.

Sample	BET (m ² /g)	l* (nm)
MnCo1.8Fe0.2	6.0±0.3	182±9
MnCo1.6Fe0.4	6.8±0.3	163±8
MnCo1.8Cu0.2	3.3±0.2	323±20
MnCo1.6Fe0.2Cu0.2	3.8±0.2	287±16

$$*l = \frac{6}{SSA \cdot \rho}$$

501

502

503 *Table 3: Sintering thermal treatments.*

Sample	Green density (%)	Sintering treatment	Sintered density (%)
MnCo1.8Fe0.2	66±1	4 h @1200°C + 4 h @800°C	92±1
MnCo1.6Fe0.4	66±1	4 h @1200°C + 4 h @800°C	90±1
MnCo1.8Cu0.2	65±1	4 h @1000°C + 4 h @800°C	97±1
MnCo1.6Fe0.2Cu0.2	65±1	4 h @1000°C + 4 h @800°C	95±1

504

505

506 *Table 4. Lattice parameter (a) of the cubic spinel cell calculated from XRD patterns of*

507 *the sintered samples.*

Sample	a (Å)
MnCo1.8Fe0.2	8.319(7)
MnCo1.6Fe0.4	8.351(8)
MnCo1.8Cu0.2	8.277(8)
MnCo1.6Fe0.2Cu0.2	8.312(8)

508

509

510 *Table 5. Thermal expansion coefficient measured between room temperature and 800°C*

511 *for the different samples.*

Sample	CTE ($\cdot 10^{-6} \text{ K}^{-1}$) [30°-800°]
MnCo1.8Fe0.2	12.7±0.1
MnCo1.6Fe0.4	11.1±0.1
MnCo1.8Cu0.2	13.7±0.1
MnCo1.6Fe0.2Cu0.2	12.9±0.1

512 *Table 6. Activation energy calculated from the Arrhenius plot of 10 hours milled*
513 *samples.*

Sample	Ea (eV)
MnCo1.8Fe0.2	0.54±0.03
MnCo1.6Fe0.4	0.53±0.03
MnCo1.8Cu0.2	0.46±0.03
MnCo1.6Fe0.2Cu0.2	0.50±0.03

514